

Fundamental Limits to Single-Photon Detection Determined by Quantum Coherence and Backaction

Steve M. Young, Mohan Sarovar, François Léonard

Sandia National Laboratories, Livermore, CA, 94551, USA

Single-photon detectors have achieved impressive performance, and have led to a number of new scientific discoveries and technological applications. Existing models of photodetectors are semiclassical in that the field-matter interaction is treated perturbatively and time-separated from physical processes in the absorbing matter. An open question is whether a fully quantum detector, whereby the optical field, the optical absorption, and the amplification are considered as one quantum system, could have improved performance. Here we develop a theoretical model of such photodetectors and employ simulations to reveal the critical role played by quantum coherence and amplification backaction in dictating the performance. We show that coherence and backaction lead to tradeoffs between detector metrics, and also determine optimal system designs through control of the quantum-classical interface. Importantly, we establish the design parameters that result in a perfect photodetector with 100% efficiency, no dark counts, and minimal jitter, thus paving the route for next generation detectors.

Modern models of photodetectors and the photodetection process are rooted in pioneering work in quantum optics and quantum electronics [1–5], and have not been significantly modified or updated since. This is surprising given the degree to which experimental photodetection technology has progressed over the past century. Indeed, single-photon photodetectors have been developed based on a wide range of physical processes that span from the photoelectric effect in semiconductors [6, 7] to superconductivity [8–10], and moreover, these photodetectors have achieved impressive performance in terms of efficiency, dark count rate, and jitter [11, 12]. Furthermore, advances in materials science and nanoscale engineering open up possibilities for not only tuning the microscopic properties and dynamics of photodetectors, but also to develop entirely new classes of photodetectors. Such possibilities motivate a re-examination of photodetection theory, with a view on understanding the fundamental limits and tradeoffs. In particular, an open question is whether a photodetector where the electromagnetic field, light-matter interaction and amplification processes are all captured within a single quantum mechanical system could reveal new regimes of photodetector performance.

In this work we present such a re-examination of photodetection by developing a fully quantum mechanical minimal model for photodetection and examining the fundamental limits that emerge from this model. Our approach relies on recent advances in quantum optics theory and quantum measurement theory. As shown in Fig. 1, the photodetection process consists of three components: (i) coherent interaction between the electromagnetic (EM) field and a localized system (usually some matter degrees of freedom), (ii) localization of information about portions of the EM field state, usually through a transfer of energy from the EM field to the localized system, and (iii) amplification of this informa-

tion to classical/macroscopic degrees of freedom. Importantly, we do not assume that the dynamics of each of these components are necessarily at different timescales and thus effectively noninteracting. Such an assumption is implicit in the traditional theory of photodetection and most subsequent treatments that treat the light-matter interaction perturbatively.

In order to simulate the dynamics of photodetection we use an open quantum systems formalism [13], and develop a master equation that explicitly accounts for the EM field degrees of freedom and internal degrees of freedom of the detector (the energy states depicted in Fig. 1). We use the formalism developed by Baragiola *et al.* [14] for modeling the interaction of few-photon wavepackets with matter. This formalism is fully quantum mechanical and therefore captures the modification of the field mode as a result of interaction with the detector. The state of the detector internal degrees of freedom at any time is given by the density matrix $\varrho(t) = \sum_{MN} c_{MN}^* \rho^{MN}(t)$, where c_{MN} are defined by an expansion of the initial state of the field in terms of Fock state wavepackets, *i.e.* $\rho_{\text{field}}(0) = \sum_{MN} c_{MN} |M_E\rangle \langle N_E|$, with $|N_E\rangle$ being an N -photon wavepacket with temporal envelope given by $E(t)$, see Methods. ρ^{MN} are auxiliary density matrices whose temporal evolution is dictated by a hierarchy of coupled differential equations [14]. In our context, to model the three components of photodetection mentioned above, these coupled equations take the form:

$$\begin{aligned} \dot{\rho}^{MN}(t) = & \mathcal{M}(\rho^{MN}(t)) + \mathcal{A}(\rho^{MN}(t)) + \{ \mathcal{D}[L](\rho^{MN}(t)) \\ & + \sqrt{M}E(t) [\rho^{M-1N}(t), L^\dagger] \\ & + \sqrt{N}E^*(t) [L, \rho^{MN-1}(t)] \} \end{aligned} \quad (1)$$

where \mathcal{M} represents the dynamics of the detector internal

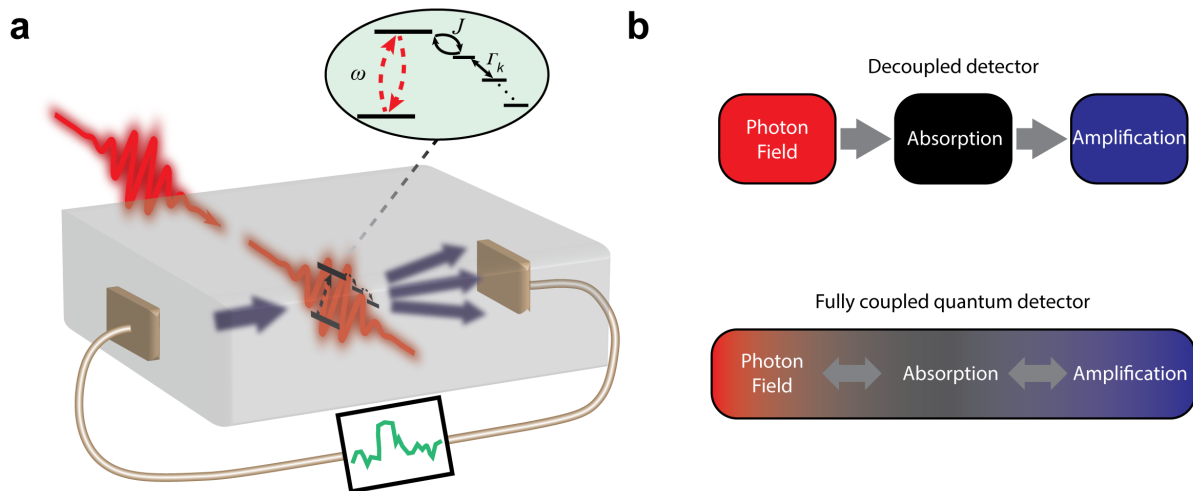


Figure 1. Single-photon detection in a fully-coupled detector. **a**, Illustration of a photodetector where photon wavepackets interact with the detector (matter) degrees of freedom. The optically coupled excited state can decay into a number of optically inactive states. Information carriers, *e.g.*, electrons, interact with the matter energy levels and scatter, causing a response that can be monitored through a measurement. **b**, The conventional theory of photodetection assumes that the photon field, the absorption process, and the amplification process occur at different timescales and can therefore be treated separately. Alternatively, in this work we consider a fully coupled model where the three subsystems are treated as being part of one quantum system.

degrees of freedom (that lead to excitation localization), \mathcal{A} represents the dynamics of the amplification process, and the remaining terms capture the field-matter excitation dynamics (L is the matter operator coupled to the field – *e.g.*, a transition operator that couples the optically active states). The superoperator \mathcal{D} is defined as $\mathcal{D}[A]\rho \equiv A\rho A^\dagger - \frac{1}{2}A^\dagger A\rho - \frac{1}{2}\rho A^\dagger A$. In the following we discuss the details of the superoperators \mathcal{M} and \mathcal{A} ; further details of this dynamical equation and its origins are presented in Methods.

The optically active internal states of the detector are coupled to a variable number of other states (that do not interact with the EM field) either coherently or incoherently. These internal states could represent *e.g.*, excitonic or electronic states of a solid-state material, or even electronic or conformational states of molecules. This coupling is captured by \mathcal{M} , which describes the dynamics of the internal states that effectively localizes a photoexcitation within the detector degrees of freedom and funnels it away from the optically active state:

$$\mathcal{M}\rho = -i[H, \rho] + \sum_k \Gamma_k \mathcal{D}[|e_{i_k}\rangle \langle e_{j_k}|] \rho. \quad (2)$$

Here, H is the Hamiltonian describing the energies of all internal states in the device (denoted $|e_l\rangle$) and coherent couplings between them; Γ_k is the incoherent transition rate from state e_{j_k} to e_{i_k} . Any incoherent transitions are a result of interactions with reservoirs, *e.g.*, phonon degrees of freedom; we do not explicitly model these here, and instead capture their net effect on the essential internal states of the detector.

Finally, \mathcal{A} represents the amplification component cap-

tured using quantum measurement theory. A designated final internal state, $|X\rangle$, is continuously monitored, a process modeled using a quantum measurement master equation that can be derived from general principles [15–17]. This monitoring effectively amplifies information about occupation of that state by generating a classical measurement record that depends on the population of the state.

The average effects of the amplification are captured by the term:

$$\mathcal{A}\rho = \chi \mathcal{D}[|X\rangle \langle X|] \rho \quad (3)$$

with χ a rate that quantifies how strongly the state is monitored, or equivalently the rate at which information about the internal states is being amplified into the classical domain. The associated average measurement current is given by

$$\bar{I}_t = \int_{t-t_m}^t \chi^2 \varrho_{XX}(t') dt', \quad (4)$$

where t_m is the integration time window, and $\varrho_{XX}(t)$ is the population of the X state given by the physical density matrix for the detector internal degrees of freedom, $\varrho(t)$. In our calculations, we chose t_m values that result in optimal performance for a given χ . Such a Markovian description of the amplification process is not universal, but importantly, it captures the fact that any amplification process must have an associated backaction on the system being amplified [18, 19]. An advantage to modeling the amplification process as a continuous measurement is that we can utilize quantum trajectory theory

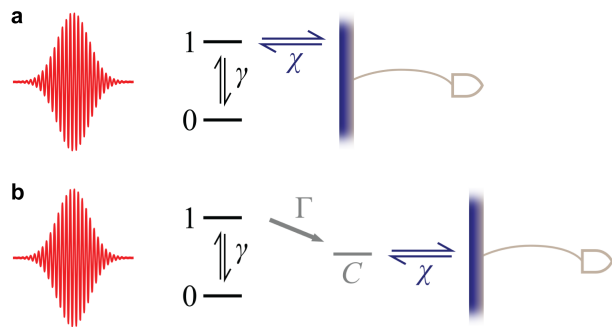


Figure 2. The two configurations under consideration. In both cases, we consider a single-photon Gaussian wavepacket (left) incident on a two-level system, creating a resonant excitation. A quantum measurement element (vertical purple line) couples to the internal states and amplifies the signal to the classical domain (right). In **a**, the quantum measurement element directly couples to the excited state and so $|X\rangle \rightarrow |1\rangle$, while in **b**, the population in the excited state may decay into a third, optically inert state to which the quantum measurement element is coupled, and so $|X\rangle \rightarrow |C\rangle$.

[17, 20] to “unravel” a measurement master equation into a stochastic master equation (SME) that enables simulation of the photodetection system conditioned on particular measurement records. This enables simulation of individual photodetection records and associated dynamics, in addition to the average record and dynamics given by Eqs. 3 and 4. The explicit form of the associated SME can be found in Methods.

The above general model applies to a broad range of physical systems. In the Supplementary Information we examine an explicit physical device for photodetection and show how one can derive a description like the one used here from physical interaction models.

Given the above minimal model of a photodetector and its dynamics, we ask several fundamental design questions: What is the best arrangement of internal states and couplings between them in order to maximize performance? Is a time-scale separation between the light-matter interaction and subsequent internal dynamics optimal? To answer such questions, it turns out to be sufficient to study two specific detector configurations: Configuration 1, with the final monitored state, $|X\rangle$, being the same as the optically active state (Fig. 2a), and Configuration 2, with $|X\rangle$ being a long-lived dark state, $|C\rangle$, to which the optically active state incoherently decays (Fig. 2(b)). In the latter configuration we assume that $|1\rangle$ and $|C\rangle$ are sufficiently separated in energy so that thermally excited population transfer from $|C\rangle$ to $|1\rangle$ can be neglected. Such a thermal effect can be modeled but would only yield a trivial decrease in efficiency of this configuration. In the following, we study both of these configurations using the dynamical model described above and quantify detector performance in terms of efficiency, dark count rates, and jitter.

We assume that the incoming field contains a single photon with a Gaussian temporal profile $|E(t)|^2 =$

$(\frac{1}{2\pi\sigma^2})^{\frac{1}{2}} e^{-\frac{t^2}{2\sigma^2}}$ of width $\sigma = 1\text{ns}$. The field-matter coupling is $L = \gamma|0\rangle\langle 1|$ with $\gamma = 0.01\text{ps}^{-1}$, which produces near-maximal absorption probability of $\approx 80\%$ for an isolated, unmonitored two-state system [21]. Since we consider an initial state containing a single photon, we need only propagate ρ^{11} , ρ^{01} , ρ^{10} and ρ^{00} .

Configuration 1. The hierarchy of dynamical equations, Eq. 1, for the system in Configuration 1 can be written in component form as

$$\begin{aligned}\dot{\rho}_{01}^{01} &= -i\omega_{01}\rho_{01}^{01} - \gamma E(t) - \frac{\gamma^2 + \chi^2}{2}\rho_{01}^{01}; & \rho_{01}^{01}(0) &= 0, \\ \dot{\rho}_{00}^{11} &= 2\gamma E(t)\rho_{01}^{01} + \gamma^2\rho_{11}^{11}; & \rho_{00}^{11}(0) &= 1, \\ \dot{\rho}_{11}^{11} &= -2\gamma E(t)\rho_{01}^{01} - \gamma^2\rho_{11}^{11}; & \rho_{11}^{11}(0) &= 0,\end{aligned}$$

with $\rho_{00}^{00} = 1$ throughout, and all other elements zero throughout.

The generation of the coherence between states $|0\rangle$ and $|1\rangle$ is damped by both the spontaneous emission back into the photon mode and decoherence due to backaction from the amplification of $|1\rangle$; this restricts the development of the excited state population. Solving the equations for different values of χ makes this concrete; stronger amplification noticeably reduces the excitation probability (Fig. 3a), a manifestation of the Zeno effect [22, 23].

Simulating individual trajectories reveals additional aspects of the tradeoff between information gain and disturbance. Figure 3b shows the excitation population and associated detector output for sample trajectories. For weak amplification, Fig. 3b, the individual trajectories are similar to the averaged case. Unfortunately, due to the weak coupling the current cannot be readily distinguished from the background noise. Stronger amplification significantly alters population evolution and produces trajectories that either completely miss or completely absorb the photon. In this case the current unambiguously distinguishes photon absorption events, but at the price of reduced efficiency due to significant perturbation of the absorption probability.

A more complete picture of impact on photodetection performance emerges after compiling the results over many trajectories. Figure 3c shows the Receiver Operating Characteristics (ROC) curve obtained from simulating 1000 trajectories with a photon and 1000 trajectories without a photon, for each value of χ . The true positive rate (TPR) corresponds to the fraction of trajectories when the detector output exceeds a pre-defined threshold in the presence of a photon in the field, while the false positive rate (FPR) is when the detector output exceeds the threshold without a photon being incident on the detector. Each point on the ROC curve is for a different value of the threshold, which decreases from left to right. For large thresholds, both the TPR and the FPR are low, while for low threshold both the TPR and the FPR are high. We find a clear tradeoff between TPR and FPR regardless of the threshold used.

We also show in the inset of Fig. 3c the efficiency as a

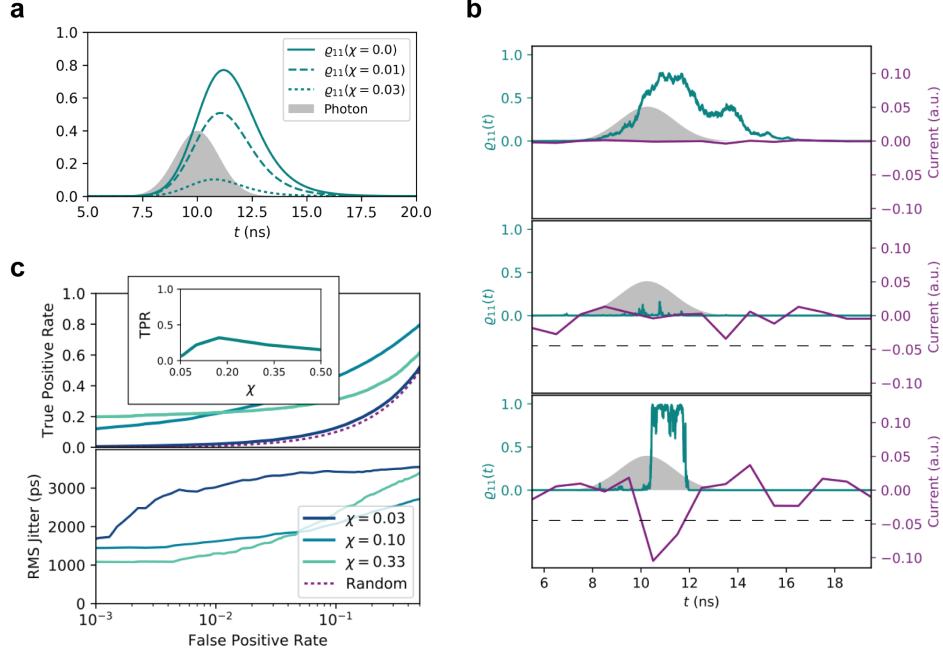


Figure 3. Detection events and performance for Configuration 1. **a**, The averaged population dynamics for Configuration 1 with amplification strengths $\chi = 0$, $\chi = 0.01\text{ps}^{-1}$, and $\chi = 0.03\text{ps}^{-1}$. The instantaneous current is proportional to $\chi^2\rho_{11}$. **b**, Sample trajectories and current outputs for $\chi = 0.00333\text{ps}^{-1}$ (top panel) and $\chi = 0.0333\text{ps}^{-1}$ (bottom two panels). The horizontal dashed lines are examples of current thresholds used to calculate the ROC curves. **c**, ROC curve and jitter vs. false positive rate, for several amplification strengths obtained by computing each for varying current thresholds for detection. The dashed line is the result for “detectors” that simply record random hits at varying rates, giving equal true positive and false positive rates. In the inset, the efficiency for a false positive rate of 0.01 is plotted as a function of χ ; optimal detection efficiency is obtained for intermediate amplification strength for a modest rate of false positives and strong amplification strength for minimal false positives. Stronger coupling also reduces jitter, which increases with the false positive rate.

function of the amplification strength χ for a fixed FPR of 0.01. As might be anticipated from the average dynamics, the efficiency is maximized for intermediate amplification strength: too weak and the signal cannot be reliably separated from the noise, too strong and excitation is suppressed. Calculation of the RMS jitter (Fig. 3c) reveals no tradeoff with dark counts: a low FPR is associated with low jitter. Unfortunately this occurs when the TPR (efficiency) is low. At the higher efficiency levels, where intermediate coupling maximizes efficiency, we find that the same intermediate coupling also gives the lowest jitter.

Ultimately, we find that directly amplifying the optical excitation interferes with the excitation itself, creating a tradeoff between increasing the signal-to-noise ratio and avoiding amplification-induced decoherence.

Configuration 2. In the case where the excited state decays to a dark state (Fig. 2b), the matrix equations become

$$\begin{aligned}\dot{\rho}_{01}^{01} &= -i\omega_{01}\rho_{01}^{01} + \gamma E(t) - \frac{\gamma^2 + \Gamma^2}{2}\rho_{01}^{01}; & \rho_{01}^{01}(0) &= 0, \\ \dot{\rho}_{00}^{11} &= 2\gamma E(t)\rho_{01}^{01} + \gamma^2\rho_{11}^{11}; & \rho_{00}^{11}(0) &= 1, \\ \dot{\rho}_{11}^{11} &= 2\gamma E(t)\rho_{01}^{01} - (\gamma^2 + \Gamma^2)\rho_{11}^{11}; & \rho_{11}^{11}(0) &= 0, \\ \dot{\rho}_{CC}^{11} &= \Gamma^2\rho_{11}^{11}; & \rho_{CC}^{11}(0) &= 0,\end{aligned}$$

with $\rho_{00}^{00} = 1$ throughout, and all other elements zero throughout. Γ is the incoherent decay rate from $|1\rangle$ to $|C\rangle$. We note that the amplification strength appears nowhere in these equations. Thus, in contrast to Configuration 1, the average dynamics exhibit no influence from amplification strength and backaction. Instead, the coupling to the decay state introduces decoherence in a similar fashion as the amplification in Configuration 1. As such, it produces a similar tradeoff: there is an optimal value for the decay rate into this state. As seen in Fig. 4a, a slow decay rate allows for high excitation probabilities but low population of the measured state, while fast decay rates convert more of the excited population into the measured-state population, but reduce the excitation probability through decoherence.

Despite the average dynamics being insensitive to the amplification strength, the relationship between information gain and disturbance is still affected by the details of the amplification. This is evident when examining individual trajectories (Fig. 4b). The strong amplification yields currents that unambiguously signal absorption or non-absorption. Moreover, in this configuration, the long lifetime of the $|C\rangle$ state results in a persistent current when the photon has been absorbed. Interestingly, although the amplification cannot influence the average

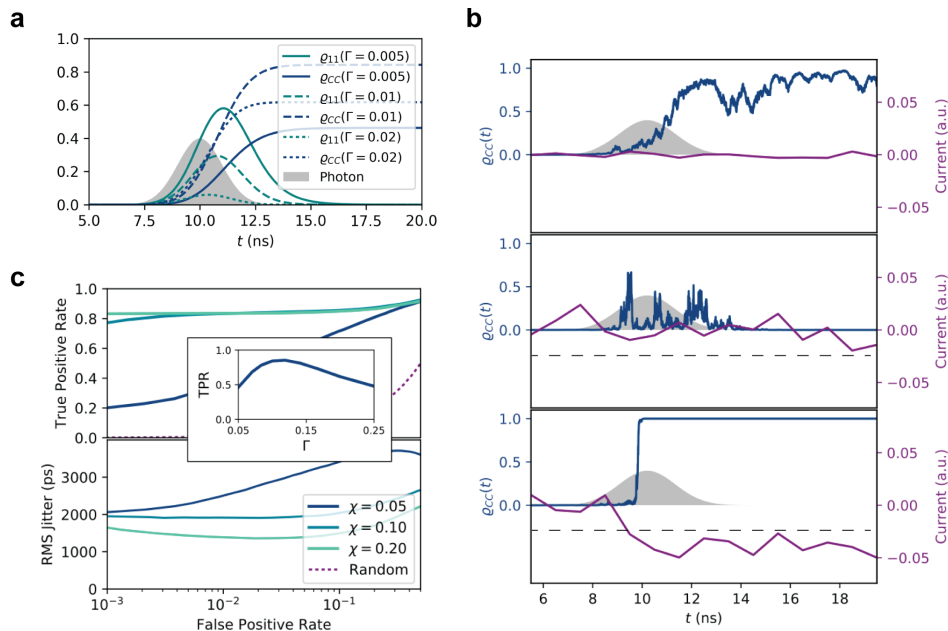


Figure 4. Detection events and performance for Configuration 2. **a**, Average population dynamics for different values of the incoherent transfer rate Γ . **b**, Sample trajectories and detector output for $\chi = 0.005 \text{ ps}^{-1}$ (top panel) and for $\chi = 0.02 \text{ ps}^{-1}$ (bottom two panels) where the photon is not absorbed and when the photon induces an excitation. The horizontal dashed lines are examples of current thresholds used to calculate the ROC curves. **c**, ROC curve and jitter vs. false positive rate for several amplification strengths. Very high detection efficiency is obtained for strong amplification at essentially no cost in terms of dark count rate or jitter. The efficiency is plotted against the rate of relaxation into the dark state Γ (inset). There is a clear maximum; faster transfer collects excitation more efficiently but inhibits the excitation process.

populations (and hence there is no Zeno effect according to traditional definitions [23]), the amplification does not affect the variance in the populations – larger χ yields a larger variance in population statistics at a fixed time.

Again, we can summarize the influence of various parameters by aggregate performance statistics (Fig. 4c). The detection efficiencies are significantly higher than for Configuration 1; moderate amplification is sufficient to guarantee optimal efficiency with negligible dark counts and no tradeoff must be negotiated. Indeed, Fig. 4c shows that for high threshold values, the TPR exceeds 0.8 while the FPR is 0.001. Similarly, jitter is much less sensitive to the detection threshold. In contrast to Configuration 1, amplification does not adversely affect optical excitation; no tradeoff exists, and both efficiency and jitter are optimized by stronger, rather than intermediate, amplification.

In the above, we have taken the optical coupling to be in the regime that provides optimal excitation probability for the isolated two state system [21]. This optimum occurs due to the tradeoff between excitation rate and emission rate. However, the introduction of an amplification mechanism adds both additional decoherence and protects against emission back into the field mode. This suggests that the detector may be able to take advantage of strong optical coupling. In addition, since our results indicate that relaxation into the $|C\rangle$ state should occur at a similar rate as the excitation, increasing the optical coupling means that the relaxation rate ought to be

increased as well, further enhancing decoherence and providing protection against emission. Indeed, we find that, in contrast to the un-monitored system, the optimal optical coupling is arbitrarily high; the detector can actually achieve near perfect efficiency if both $\gamma \gg 1/\sigma$ and $\gamma = \Gamma$, as shown in Fig. 5. Essentially, the pulse is absorbed as quickly as possible and the resulting excited state population is shunted to the dark state as soon as it develops, preventing re-emission. Additionally, the amplification can be made arbitrarily strong, since the coherent field-matter interaction is decoupled from its backaction by the incoherent decay process, so that dark counts can be essentially eliminated. Performing 50,000 simulations with and without a photon using $\gamma = \Gamma = 0.1 \text{ ps}^{-1}$, we find that a wide range of thresholds yield 50,000 hits, 0 dark counts, and 1.05ns of jitter, where 1.0ns jitter is the lower limit set by the wavepacket width, σ . Furthermore, almost perfect detection is possible for a wide range of single-photon pulse widths – *e.g.*, for the value $\gamma = \Gamma = 0.1 \text{ ps}^{-1}$, such ideal performance holds for pulses as short as 100ps (see Supplementary Information for additional trajectories). For shorter pulses, efficiency is reduced (Fig. 5), as absorption no longer occurs rapidly enough to collect the entire pulse.

This demonstrates that tradeoffs in photodetection can be circumvented through detector design, and that a perfect detector is in principle possible.

At the most general level, the two models discussed here represent all the detectors of the kind presented in

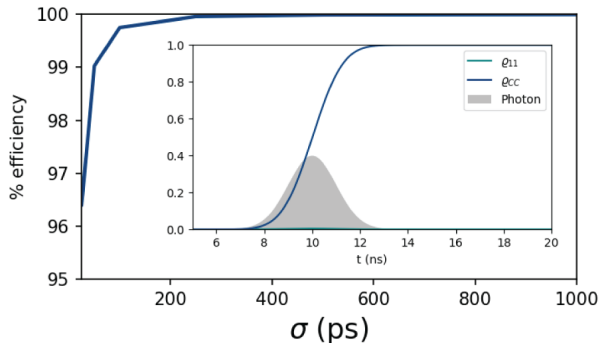


Figure 5. Perfect photodetector. The average dynamics of Configuration 2 with $\gamma = \Gamma = 0.1\text{ps}^{-1}$. Strong optical coupling means that excitation occurs rapidly compared to the pulse duration, and a matched rate of incoherent transfer converts excited state population to dark state population as soon as the former develops. Consequently, regardless of the strength of the quantum measurement, the measured state $|C\rangle$ attains 100% probability and the excited state $|1\rangle$ is nearly unoccupied throughout.

Fig. 1.

The presence of multiple decay states and/or extended decay pathways does not qualitatively alter our results, to the extent that final states are all monitored; decay processes to unmonitored states will obviously and straightforwardly limit performance.

Finally, we believe that current high-performance single-photon detectors should be described by Configuration 2. Both avalanche photodiodes and superconducting detectors rely on rapid incoherent decay from an optically excited coherent state to optically inert intermediate states before amplification. Our results clearly show why these types of detectors offer the superior performance they are known for, and suggest that in principle this class of detectors may be tuned to operate perfectly, providing a fundamental design principle for guiding future efforts to engineer new photodetector types regardless of the underlying physical mechanisms.

Methods

To model the photon wavepacket and its interaction with the system, we adopt the approach of Ref. [14]. In the case of a propagating wavepacket with carrier frequency resonant with a localized system coupled to the field, the state of the localized system can be represented by the density matrix $\varrho(t) = \sum_{MN} c_{MN}^* \rho^{MN}(t)$, where c_{MN} are defined by an expansion of the initial state of the field in terms of Fock state wavepackets, *i.e.* $\rho_{\text{field}}(0) = \sum_{MN} c_{MN} |M_E\rangle \langle N_E|$, with $|N_E\rangle = 1/\sqrt{N!} [\int ds E(s) b^\dagger(s)]^N |0\rangle$ being an N -photon wavepacket (or continuous-mode Fock state) with temporal envelope given by $E(t)$. Under a Markov approximation for the field-matter interaction one may derive from the Ito Langevin equation a hierarchy of master equations for the auxiliary density matrices:

$$\begin{aligned} \dot{\rho}^{MN}(t) &= \mathcal{M}\rho^{MN}(t) + \mathcal{L}_t^{MN}\rho^{MN}(t) \\ &= \mathcal{M} + \mathcal{D}[L](\rho^{MN}) + \sqrt{M}E(t) [\rho^{M-1N}, L^\dagger] \\ &\quad + \sqrt{N}E^\dagger(t) [L, \rho^{MN-1}] \end{aligned}$$

where \mathcal{M} represents free evolution of the localized system and L is an operator on the localized system that couples to the field. For all auxiliary density matrices where $N = M$, the initial state is the physical initial state of the localized system, while all other auxiliary density matrices are initialized to zero.

The formalism developed in Ref. [14] assumes the field mode propagates along a 1D waveguide. The extension to 3D propagation may be done without much difficulty, but we do not consider it here. Also, the resonant interaction assumption is not necessary, one could generalize to interaction with several two-level systems of various detunings with respect to the field mode.

The inclusion of amplification adds the term \mathcal{A} to the master equations, so that in the case of a single-photon wavepacket (where we only have auxiliary density matrices up to $N = M = 1$) and real electric field $E(t)$, we have

$$\begin{aligned} \dot{\rho}^{11} &= -i[H, \rho^{11}] + E(t) ([\rho^{01}, L^\dagger] + [L, \rho^{10}]) \\ &\quad + \mathcal{D}[L]\rho^{11} + \chi^2 \mathcal{D}[|X\rangle \langle X|]\rho^{01} \\ \dot{\rho}^{01} &= -i[H, \rho^{01}] + E(t)[L^\dagger, \rho^{00}] \\ &\quad + \mathcal{D}[L]\rho^{01} + \chi^2 \mathcal{D}[|X\rangle \langle X|]\rho^{01} \\ \dot{\rho}^{00} &= -i[H, \rho^{00}] + \mathcal{D}[L]\rho^{00} + \chi^2 \mathcal{D}[|X\rangle \langle X|]\rho^{01} \end{aligned}$$

where H is the free Hamiltonian for the system.

These equations describe the average or unmonitored state of the system. The conditional dynamics, in which the detector output influences the subsequent system dynamics, are obtained by the addition of the nonlinear term [20]

$$\begin{aligned} \chi \mathcal{H}[|X\rangle \langle X|]\rho^{MN} dW(t) \\ \equiv \chi \left(|X\rangle \langle X| \rho^{MN} + \rho^{MN} |X\rangle \langle X| \right. \\ \left. - 2\langle |X\rangle \langle X| \rangle_{\varrho(t)} \rho^{MN} \right) \frac{dW(t)}{dt}, \end{aligned}$$

to each of the evolution equations in the hierarchy, resulting in a set of stochastic differential equations. $dW(t)$ is a Wiener increment (Gaussian distributed random variable with mean zero and variance dt). We note that the expectation value $\langle |X\rangle \langle X| \rangle_{\varrho(t)}$ is evaluated under the physical density matrix $\varrho(t)$; this expectation value is used to evaluate $\mathcal{H}[|X\rangle \langle X|]\rho^{MN}$ for the evolution of the auxiliary density matrices as well. As a consequence, only the trace of the real density matrix is conserved; the traces of the auxiliary matrices are not. This is necessary to correctly reflect the conditioning of the density matrix outcome on the measurement process.

The observed current consistent with this state evolution is given by

$$I_t = \int_{t-t_m}^t \chi^2 \varrho_{XX}(t') dt' + \chi dW(t').$$

We numerically solved the above equations using the order (2.0,1.5) stochastic Runge-Kutta algorithm proposed in Ref. [24]. We perform simulations of the output signal when a photon is, or is not, incident on the detector, and for a given threshold value of integrated current, record hits, misses, dark counts, and jitter. For each set of parameters considered we performed 1000 simulations with incident photons and 1000 without, from which we extract true positive rates (percentage of the time a hit is recorded when a photon is present), false positive rates (percentage of the time the current exceeds the threshold when a photon is absent), and jitter (standard deviation of the time a hit is recorded with respect to photon arrival time). In the case of the perfect detector we extended these simulations to 50000 events in order to observe any extremely rare probability events.

REFERENCES

- [1] Glauber, R. J. Photon correlations. *Phys. Rev. Lett.* **10**, 84–86 (1963).
- [2] Kelley, P. L. & Kleiner, W. H. Theory of Electromagnetic Field Measurement and Photoelectron Counting. *Phys. Rev.* **136**, A316–A334 (1964).
- [3] Scully, M. O. & Lamb, W. E. Quantum Theory of an Optical Maser. III. Theory of Photoelectron Counting Statistics. *Phys. Rev.* **179**, 368–374 (1969).
- [4] Ueda, M. Nonequilibrium open-system theory for continuous photodetection processes: A probability-density-functional description. *Phys. Rev. A* **41**, 3875–3890 (1990).
- [5] Mandel, L. & Wolf, E. *Optical Coherence and Quantum Optics* (Cambridge University Press, 1995).
- [6] Bienfang, J. C. *et al.* Quantum key distribution with 1.25 Gbps clock synchronization. *Optics Express* **12**, 2011 (2004).
- [7] Woodson, M. E. *et al.* Low-noise AlInAsSb avalanche photodiode. *Applied Physics Letters* **108**, 081102 (2016).
- [8] Pernice, W. H. P. *et al.* High-speed and high-efficiency travelling wave single-photon detectors embedded in nanophotonic circuits. *Nature* **3**, 1325 (2012).
- [9] Marsili, F. *et al.* Efficient Single Photon Detection from 500 nm to 5 μm Wavelength. *Nano. Lett.* **12**, 4799–4804 (2012).
- [10] Marsili, F. *et al.* Detecting Single Infrared Photons with 93% System Efficiency. *Nature Photonics* **7**, 210 (2013).
- [11] Eisaman, M. D., Fan, J., Migdall, A. & Polyakov, S. V. Invited Review Article: Single-photon sources and detectors. *Review of Scientific Instruments* **82**, 071101 (2011).
- [12] Hadfield, R. H. Single-photon detectors for optical quantum information applications. *Nat. Photon.* **3**, 696–705 (2009).
- [13] Breuer, H.-P. & Petruccione, F. *The theory of open quantum systems* (Oxford University Press, 2002).
- [14] Baragiola, B. Q., Cook, R. L., Branczyk, A. M. & Combes, J. N-photon wave packets interacting with an arbitrary quantum system. *Phys. Rev. A* **86**, 013811 (2012).
- [15] Caves, C. M. & Milburn, G. J. Quantum-mechanical model for continuous position measurements. *Phys. Rev. A* **36**, 5543 (1987).
- [16] Cresser, J. D., Barnett, S. M., Jeffers, J. & Pegg, D. T. Measurement master equation. *Optics Communications* **264**, 352–361 (2006).
- [17] Jacobs, K. & Steck, D. A. A straightforward introduction to continuous quantum measurement. *Contemp. Phys.* **47**, 279 (2006).
- [18] Caves, C. M. Quantum limits on noise in linear amplifiers. *Phys. Rev.* **26**, 1817–1839 (1982).
- [19] Clerk, A. A., Girvin, S. M., Marquardt, F. & Schoelkopf, R. J. Introduction to quantum noise, measurement, and amplification. *Rev. Mod. Phys.* **82**, 1155–1208 (2010).
- [20] Wiseman, H. M. & Milburn, G. J. *Quantum measurement and control* (Cambridge University Press, 2009).
- [21] Wang, Y., Minář, J., Sheridan, L. & Scarani, V. Efficient excitation of a two-level atom by a single photon in a propagating mode. *Phys. Rev. A* **83**, 063842–6 (2011).
- [22] Misra, B. & Sudarshan, E. C. G. The Zeno’s paradox in quantum theory. *J. Math. Phys.* **18**, 756 (1977).
- [23] Facchi, P. & Pascazio, S. Quantum Zeno and inverse quantum Zeno effects. *Prog. Optics* **42**, 147 (2001).
- [24] Röckler, A. Runge–kutta methods for the strong approximation of solutions of stochastic differential equations. *SIAM Journal on Numerical Analysis* **48**, 922–952 (2010).
- [25] Zhou, X. *et al.* Color detection using chromophore-nanotube hybrid devices. *Nano Letters* **9**, 1028–1033 (2009).
- [26] Goan, H.-S., Milburn, G. J., Wiseman, H. M. & Bi Sun, H. Continuous quantum measurement of two coupled quantum dots using a point contact: A quantum trajectory approach. *Phys. Rev. B* **63**, 125326 (2001).

Acknowledgments

Work supported by the DARPA DETECT program. Sandia National Laboratories is a multimission laboratory managed and operated by National Technology and Engineering Solutions of Sandia, LLC., a wholly owned subsidiary of Honeywell International, Inc., for the U.S. Department of Energy’s National Nuclear Security Administration under contract DE-NA-0003525.

Supplementary Information: Fundamental Limits to Single-Photon Detection Determined by Quantum Coherence and Backaction

Steve M. Young, Mohan Sarovar, François Léonard

Sandia National Laboratories, Livermore, CA, 94551, USA

1. Example derivation of master equation from physical system

In this section we derive a stochastic master equation representing a concrete physical system to illustrate the general formalism presented in the main text. Figure 6 shows a schematic of the “device” for which we will write a dynamical model. It consists of a photoactive molecule positioned near a short-channel ((*e.g.*, 10nm) carbon nanotube (CNT) connected to leads. There are three relevant states in the molecule: the ground state $|0\rangle$, an excited state $|1\rangle$ optically connected to the ground state, and an optically dark state $|C\rangle$ that represents the state of the molecule after photon absorption, such as can arise from photoisomerization. The static dipole of the molecule is different (in magnitude and direction) in states $|1\rangle$ and $|C\rangle$ and this change induces a change in the electrostatic potential of the CNT and as a result, the current across it. Such systems have been previously studied experimentally [25].

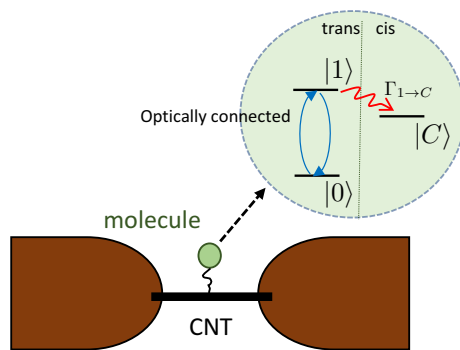


Figure 6. A schematic of a molecular photodetection device. Photons are absorbed by the molecular system (internal structure shown), and the detection event is amplified by electronic transport in the carbon nanotube. A quantum measurement master equation for the dynamics of this device is developed in this section.

In order to develop a model for this device, we will approximate the transport of electrons across the nanotube as a tunneling process, which is justified by the short channel length. The tunnel barrier is set by the energy levels in the nanotube. Given this simplification, we can model the system using a Hamiltonian $H = H_f + H_{f-m} + H_m + H_{m-CNT} + H_{CNT}$, where H_f, H_m and H_{CNT} are the bare electromagnetic (EM) field, molecule and CNT Hamiltonians, respectively. H_{f-m} is the field-molecular interaction, and H_{m-CNT} is the molecule-CNT interaction. Explicitly, these Hamiltonians are:

$$\begin{aligned}
 H_m &= \hbar\omega_0 |0\rangle \langle 0| + \hbar\omega_1 |1\rangle \langle 1| + \hbar\omega_C |C\rangle \langle C| \\
 H_{CNT} &= \sum_k (\hbar\omega_k^L a_{Lk}^\dagger a_{Lk} + \hbar\omega_k^R a_{Rk}^\dagger a_{Rk}) + \sum_{k,q} (T_{kq} a_{Lk}^\dagger a_{Rq} + T_{qk}^* a_{Rq}^\dagger a_{Lk}) \\
 H_{m-CNT} &= \sum_{k,q} |C\rangle \langle C| (\chi_{kq} a_{Lk}^\dagger a_{Rq} + \chi_{qk}^* a_{Rq}^\dagger a_{Lk}).
 \end{aligned} \tag{5}$$

We will leave H_f and H_{f-m} unspecified at this point. In the above, $\hbar\omega_0, \hbar\omega_1, \hbar\omega_C$ are the energies of the respective states of the molecule. $\hbar\omega_k^L$ and $\hbar\omega_k^R$ are the energies of left and right reservoir/lead states at wavenumber k , and a_{Lk}, a_{Rk} are (fermionic) annihilation operators for these states. T_{kq} is the tunneling matrix element between states k and q in the left and right reservoir, and χ_{kq} is the perturbation to this element due to the molecule being in state $|C\rangle$. Note that this effectively means that the tunneling amplitude goes from T_{kq} to $T_{kq} + \chi_{kq}$ when the molecule is in the $|C\rangle$ state.

In addition to these coherent dynamics, the different conformational states $|1\rangle$ and $|C\rangle$ are connected by an incoherent rate $\Gamma_{1\rightarrow C}$ (and we assume the backward transition rate $\Gamma_{C\rightarrow 1}$ is negligible).

This model for the CNT and molecule-CNT interaction are similar to the model used for quantum point contact based measurement in Ref. [26]. Following that reference, we can now derive a master equation describing the dynamics of the molecule and light degrees of freedom only by integrating out the continuum of reservoir states:

$$\begin{aligned}\dot{\varrho}(t) &= -\frac{i}{\hbar} [H_f + H_{f-m} + H_m, \varrho] + \Gamma_{1\rightarrow C} \mathcal{D}[|C\rangle \langle 1|] \varrho(t) + \mathcal{D}[\mathcal{T}_+ + \mathcal{X}_+ |C\rangle \langle C|] \varrho(t) + \mathcal{D}[\mathcal{T}_-^* + \mathcal{X}_-^* |C\rangle \langle C|] \varrho(t) \\ &\equiv -\frac{i}{\hbar} [H_f + H_{f-m} + H_m, \varrho] + \mathcal{L}_t \varrho\end{aligned}\quad (6)$$

where ϱ is the density matrix for the molecular and field degrees of freedom only. In this equation, \mathcal{D} is a superoperator defined as:

$$\mathcal{D}[A]\rho = A\rho A^\dagger - \frac{1}{2} A^\dagger A\rho - \frac{1}{2} \rho A^\dagger A \quad (7)$$

Before specifying the coefficients \mathcal{T}_\pm and \mathcal{X}_\pm we repeat from Ref. [26] all the assumptions that go into deriving this master equation:

1. The left and right reservoirs/leads are thermal equilibrium free electron baths.
2. Weak coupling between molecule and CNT, which effectively means that we can restrict ourselves to a second order expansion in χ_{kq}, T_{kq} .
3. The transport through the channel (CNT/QPC) is in the tunnel junction limit – *i.e.*, low transmittivity.
4. The initial state of the molecule and CNT are uncorrelated/factorizable.
5. Fast relaxation of the reservoirs – *i.e.*, the degrees of freedom in the reservoirs relax to equilibrium much faster than any system timescales.
6. Markovian approximation of the reservoir.
7. If eV is the external bias applied across the transport channel, and μ_L, μ_R are the chemical potentials in the left and right reservoirs (*i.e.*, $eV = \mu_L - \mu_R$), then $|eV|, k_B T \ll \mu_{L(R)}$.
8. Energy independent tunneling amplitudes and density of states over the bandwidth $\max(|eV|, k_B T)$.

Under these approximations, the dynamics of the system is described by the above master equation, with the coefficient determined by

$$\begin{aligned}|\mathcal{T}_\pm|^2 &= \frac{2\pi e}{\hbar} |T_{00}|^2 g_L g_R V_\pm \\ |\mathcal{T}_\pm + \mathcal{X}_\pm|^2 &= \frac{2\pi e}{\hbar} |T_{00} + \chi_{00}|^2 g_L g_R V_\pm,\end{aligned}\quad (8)$$

where T_{00}, χ_{00} are the energy-independent tunneling amplitudes near the average chemical potential, g_L, g_R are the energy-independent density of states in the left and right reservoirs, respectively. The finite temperature effective external bias is:

$$eV_\pm \equiv \frac{\pm eV}{1 - \exp\left(\frac{\mp eV}{k_B T}\right)} \quad (9)$$

At first approximation, we can work in the limit of low temperature and ignore the thermally activated current in the reverse direction, and set $V_- = 0$, which will effectively remove the third term in 6.

Eq. 6 can be interpreted as a measurement master equation giving the averaged dynamics when the population in the state $|C\rangle$ is continuously monitored [26]. Conditioned dynamics, based on particular values of the current can also be derived from the corresponding stochastic master equation [20]:

$$d\varrho(t) = -\frac{i}{\hbar} [H_f + H_{f-m} + H_m, \varrho] dt + \mathcal{L}_t \varrho dt + \mathcal{H}[\mathcal{T}_+ + \mathcal{X}_+ |C\rangle \langle C|] \varrho(t) dW_+(t) + \mathcal{H}[\mathcal{T}_-^* + \mathcal{X}_-^* |C\rangle \langle C|] \varrho(t) dW_-(t),$$

where $\mathcal{H}[A]\varrho \equiv A\varrho + \varrho A^\dagger - \langle A + A^\dagger \rangle_\varrho \varrho$, and $dW_+(t)$ and $dW_-(t)$ are Wiener increments. Increments in the forward and reverse current consistent with this evolution are given by:

$$\begin{aligned}dI_+(t) &= \langle \mathcal{T}_+ + \mathcal{X}_+ |C\rangle \langle C| \rangle_\varrho dt + dW_+(t), \\ dI_-(t) &= \langle \mathcal{T}_-^* + \mathcal{X}_-^* |C\rangle \langle C| \rangle_\varrho dt + dW_-(t),\end{aligned}$$

2. Quantum trajectories for perfect detector In this section we present additional trajectories for the "perfect photodetector" for different values of the photon wavepacket width. Figure S2 shows that for pulse widths ranging from 100ps to 1ns the collection efficiency is 100%.

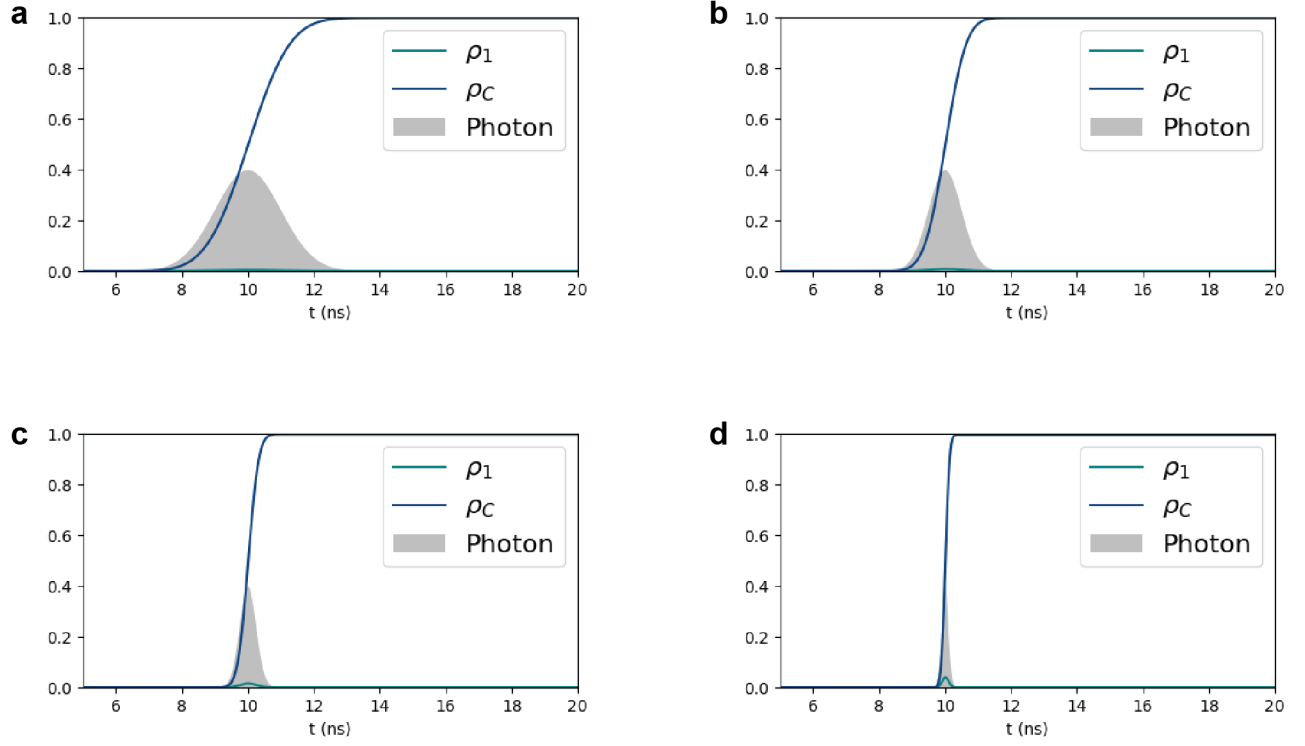


Figure 7. The average dynamics of the tree state system with $\gamma = \Gamma = 0.1\text{ps}^{-1}$ for wavepackets of widths **a**, 1ns, **b**, 500ps, **c**, 250ps, and **d**, 100ps. We see that in all cases the photon is collected 100% of the time.